Near wake behavior of an asymmetric wind turbine rotor

Pin Chun Yen[1], Wei Yu[1], and Fulvio Scarano[1]

[1]Faculty of Aerospace Engineering, Delft University of Technology, Kluyverweg 1, 2629 HS Delft

Correspondence: Wei Yu (w.yu@tudelft.nl)

Abstract. With symmetric rotors, tip vortex helices develop regularly before interacting, following the leapfrogging instability. This instability can occur earlier when the helices are radially offset by using blades of different lengths. This study investigates the spatio-temporal development of near-wake behavior for rotors with a significant blade length difference. Large eddy simulations with an actuator line model were conducted on a modified NREL 5MW wind turbine under both laminar and turbulent inflow conditions, to evaluate the impact of blade length differences ranging from 5 to 30%. The study analyzed the development of tip vortex helices, the onset of leapfrogging, vortex merging, and, ultimately, their three-dimensional breakdown. The analysis is corroborated using a simplified two-dimensional point vortex model. The results show that the leapfrogging process begins immediately downstream of the vortex release when blades of different lengths are considered. The instability growth rate obtained from the 2D vortex model agrees with the LES results. Although the rotor asymmetry accelerates the leapfrogging and, in some conditions, also the vortex merging process, it proves insufficient to cause a large-scale breakdown of the helix system and, therefore, enhance wake recovery. Inflow turbulence, however, plays a larger role in wake recovery, promoting the breakdown of tip helical vortices regardless of rotor symmetry.

1 Introduction

Wind farms, clusters of wind turbines, often face a challenge known as the wake effect. This phenomenon occurs when wakes produced by upstream turbines interact with downstream ones, which are immersed in a stream with lower kinetic energy along with an increased level of fluctuations, in turn causing a power loss and increased fatigue loads. The wake could take more than $50\,\mathrm{km}$ to recover to the freestream (Lundquist et al., 2018), which limits the turbine spacing in wind farm designs. This motivates research into methods for enhancing wake recovery, aiming to optimize wind farm layout and improve overall efficiency.

The wake recovery process occurs through the mixing with the ambient flow (van Kuik et al., 2016). The low-momentum region past the actuator is bounded by a shear layer, in the early stage comprising the helical vortices shed from the tip. This flow structure has been found to inhibit the mixing process (Medici, 2005). Furthermore, wind tunnel experiments (Lignarolo et al., 2015) have shown that in the near-wake region, fluxes of kinetic energy are quasi zero-mean, being dominated by periodic fluctuation, where the transport occurs both into and out of the wake at similar rates. Consequently, the net entrainment of kinetic energy does not increase by random turbulence until the leapfrogging zone, where tip vortex pairs exchange their

streamwise positions. In this zone, more efficient mixing from random flow motion contributes to wake recovery (Lignarolo et al., 2015).

Previous studies have explored the various methods to impose small disturbances to achieve an earlier onset of the leapfrogging phenomenon, assuming that the latter would accelerate the wake recovery. These methods can be categorized into active and passive. An example of the former is documented in the work of Ivanell et al. (2010), who introduced a small sinusoidal perturbation at the tip regions. Subsequently, Odemark and Fransson (2013) arranged two pulsed jets behind the nacelle on a small-scaled turbine in a wind tunnel experiment. Huang et al. (2019) investigated the influences of two oscillating flaps near the tip and at mid-span on the tip vortex growth rate using LES. Quaranta et al. (2015) experimentally studied the relationship between instability growth rate and wave number by adjusting the rotational speed of a single-bladed rotor. Additionally, van der Hoek et al. (2022) showed the potential of the concept of dynamic individual pitch control. Brown et al. (2022) advanced further to apply the oscillation on both rotational frequency and blade pitch.

The passive method has mostly involved the modification of rotor symmetry. Quaranta et al. (2019) conducted experiments in a water channel using a two-bladed rotor, with one blade having a 1.5% radial offset. The resulting instability growth rate based on the displacement of the tip vortex cores aligns with the theoretical predictions by Gupta and Loewy (1974). Furthermore, the leapfrogging location and tip speed ratio relation were fitted to the linear model by Sarmast et al. (2014) under different tip speed ratios. Later, the results were compared with the numerical studies by Abraham et al. (2023a). They employed the periodic point vortex method introduced by Aref (1995) and the vortex filament model by Leishman et al. (2002), concluding that the former can capture the non-linear dynamics under the vortex core size and separation of a normal wind turbine operation. Similarly, Schröder et al. (2022); Abraham and Leweke (2023) introduced blade add-ons, such as winglets or fins, to induce rotor asymmetry. Then, Abraham et al. (2023b) broadened their study from vortex dynamics to wake recovery by using the multi-fidelity vortex method solver (Ramos-García et al., 2023) to investigate leapfrogging caused by a 2% rotor asymmetry. Their findings revealed an 11% increase in available power to downstream turbines under laminar inflow conditions.

From these prior studies, it was concluded that minor radial offsets can accelerate the development of leapfrogging instability. However, a blade length difference of less than 3% may result from blade imperfections (Quaranta et al., 2015), and the effect of inflow conditions on the wake of an asymmetric rotor remains underexplored. Therefore, we expand the research to examine more macroscopic rotor asymmetry under varying inflow conditions to assess its potential and limitations using high-fidelity simulations.

The primary objective of this paper is to investigate the behavior of the near wake of a wind turbine that operates with an asymmetric rotor, focusing on the tip vortices across a range of blade length differences varying from 0% to 30% of the radius. In addition, the study aims to connect the local effects at the shear layer, with the global behavior of the wake, its recovery in particular. The relationship between rotor asymmetry and its potential benefits for wake recovery under both laminar and turbulent inflow conditions are explored to this end. To achieve these objectives, the flow field produced by the wind turbine is simulated using the large eddy simulation combined with the actuator line method. The article is structured as follows: Section 2 introduces the numerical methods and simulation setups. In Sect. 3, a 2D vortex model is presented that allows an

analytical treatment of the growth rate leading to the leapfrogging phenomenon. The spatio-temporal behavior of the shear layer dominated by the tip vortices is presented in Sect. 4, whereas the axial evolution of the wake momentum and its recovery are discussed in 5. The overall impact of rotor asymmetry, vortex leapfrogging, and merging onto the wake recovery are summarized in the Conclusions.

65 ## 2 Methodologies

2.1 Large eddy simulation and Smagorinsky model

Computations were performed using Large eddy simulations (LES) implemented in the open-source toolbox `OpenFOAM v2106` (OpenFOAM Foundation, 2021). The flow was assumed incompressible, with gravitational, Coriolis force, and thermal effects neglected. The resulting spatially filtered Navier-Stokes equation governing the flow is presented in Eq. 1, where ν_{sgs}

70 denotes the subgrid-scale viscosity. To solve the well-known closure problem, the modeling of ν_{sgs} is required. At a sufficiently high resolution of the actuator line, particularly exceeding 30 mesh points per line, the differences between various models were found to be less significant (Sarlak et al., 2015). Therefore, this study employs the Smagorinsky model (Smagorinsky, 1963), which applies the mixing length theory and eddy viscosity approximation. As shown in Eq. 2, it considers the local grid size Δ as the length scale and the shear strain rate S_{ij} as the temporal scale and has the advantage of the simplicity of its constant

75 coefficients, with $C_k = 0.094$ and $C_\epsilon = 1.048$ (Jha et al., 2014; Onel and Tuncer, 2021; Mendoza et al., 2019).

$$\frac{\partial u_i}{\partial x_i} = 0, \quad \frac{\partial u_i}{\partial t} + u_j \frac{\partial u_i}{x_j} = -\frac{1}{\rho}\frac{\partial p}{\partial x_i} + \frac{\partial}{\partial x_j}[(\nu + \nu_{\mathrm{sgs}})(\frac{\partial u_i}{\partial x_j} + \frac{\partial u_j}{\partial x_i})] + \frac{f_{\mathrm{body},i}}{\rho} \tag{1}$$

$$\nu_{\mathrm{sgs}} = C_k \sqrt{\frac{C_k}{C_\epsilon}} \Delta^2 \sqrt{2 S_{ij} S_{ij}}, \quad S_{ij} = \frac{1}{2}(\frac{\partial u_i}{\partial x_j} + \frac{\partial u_j}{\partial x_i}) \tag{2}$$

2.2 Wind turbine model

In this study, the rotor is modeled using the Actuator Line Method (ALM), originally developed by Sørensen and Shen (2002).

80 This approach models the rotor by replacing the blade geometry with actuator lines composed of discretized blade elements, depicted in Fig. 1(a). This allows the solver to bypass the need to resolve the boundary layer, distributing more computational resources to the wake region. As shown in Fig. 1(b), at each blade element the aerodynamic loading is determined based on 2D tabulated airfoil data and the local inflow conditions using Eq. 3. The resultant forces are then projected onto the flow field as body forces in a 3D Gaussian manner to avoid spatial singularities by Eq. 4.

85 $$\boldsymbol{f}_{2D} = \frac{1}{2}\rho U_a^2 c(C_L(\alpha)\boldsymbol{e}_L, C_D(\alpha)\boldsymbol{e}_D) \tag{3}$$

$$\boldsymbol{f}_{\mathrm{body},d} = \sum_{k=1}^{N_b} \int_0^R F_1(r)\boldsymbol{f}_{2D}(r)\eta_\epsilon(d)dr, \quad \eta_\epsilon = \frac{1}{\epsilon^2 \pi^{3/2}} e^{(d/\epsilon)^2} \tag{4}$$
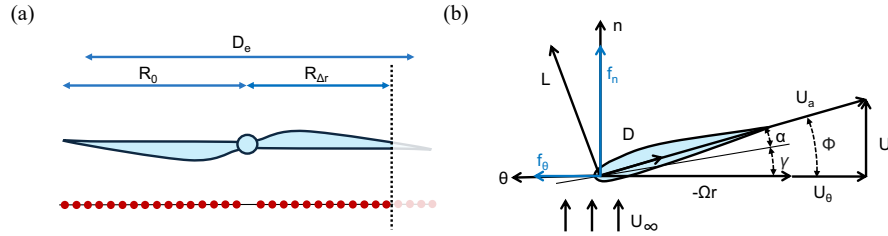
WIND
ENERGY
SCIENCE
DISCUSSIONS

Figure 1. (a):Diagram of the modified rotor, effective diameter, and its implementation on an actuator line model. (b):Diagram of a cross-sectional blade element on an actuator line with velocity and force vectors

Here, r stands for the radial position, N_b marks the number of blades, $F_1(r)$ represents the end effect correction, and η_ϵ denotes the regularization kernel. This kernel controls the distribution by the distance from actuator elements to grid centroid d and the smoothing factor ϵ.

The ALM is implemented with an `OpenFOAM` library `turbineFoam`, developed by (Bachant et al., 2019). As pointed out by Jha et al. (2014), the most important ALM parameters are ϵ, grid spacing Δ, and the discretization of the actuator line Δ_b. First, the blade is discretized into 40 elements with a uniform spacing, with Δ_b slightly smaller than Δ. This ensures the continuous force distribution along the blade (Martínez-Tossas et al., 2015). Then, following Troldborg (2009), the smoothing factor is set $\epsilon = 2\Delta_b$ as a compromise that mitigates numerical oscillation while preserving the tip vortex structure. Moreover, the original Shen correction (Shen et al., 2005) was employed to account for the inherent over-prediction of blade tip loading using ALM (Sarlak et al., 2016; Sørensen et al., 2016).

The NREL 5MW turbine (Jonkman et al., 2009) was chosen as the reference wind turbine. The original design features a 3-bladed rotor with 63m each. To focus more specifically on vortex pairing phenomena, the number of blades was reduced to two, positioned directly opposite each other. While this modification impacts induction and overall performance, the tip vortex pairing motion analysis remains valid as long as key parameters related to the leapfrogging instability, such as vortex separation distance and circulation, are controlled. Besides, the tower, nacelle, and ground effects are neglected, ensuring that the only asymmetry present is the rotor itself.

2.3 Simulation setups

2.3.1 Boundary condition and flow properties

The air is modeled as incompressible and Newtonian, with a density of $\rho = 1.225$ kgm^{-3} kinematic viscosity of $\nu = 1.5 \times 10^{-5}$ m^{2}s^{-1}. The laminar inflow is specified with a Dirichlet condition, setting the velocity at $U_\infty = 11.4$ ms^{-1}. Slip conditions, also set with U_∞ are applied to the lateral boundaries. At the outlet, a convective outflow condition $\frac{D}{Dt} = 0$ is prescribed to ensure mass conservation and to avoid disturbance evolving upstream (Troldborg, 2009). The rotor is set to operate at a tip speed ratio of $\lambda = \Omega R_0 / U_\infty = 7$, and no controller is applied for simplicity.

$$T_i = \frac{\sqrt{\frac{1}{3}(\sigma_u^2 + \sigma_v^2 + \sigma_w^2)}}{\overline{u}} \times 100\% \tag{5}$$

To better approach a realistic scenario, besides the laminar inflow condition, inflow turbulence has been set using the divergent-free synthetic eddy method (Poletto et al., 2013), implemented by `turbulentDFSEMInlet` function. As shown in Eq. 5, the turbulence intensity T_i is determined by mean velocity $\overline{u}$ and its standard deviations σ_i, measured at the rotor plane with 13 probes (Li et al., 2024). Two turbulence intensity levels were set to simulate different scenarios: a minor level of 0.5% and an atmospheric boundary layer level of 5%, representing a typical inflow condition for offshore wind farms (Hansen et al., 2012; Troldborg et al., 2011).

2.3.2 Spatial and temporal discretization

The grid layout follows the setups of Li et al. (2024), as shown in Fig. 2. The overall computational domain is set for $12.5D_0 \times 5D_0 \times 5D_0$, the Cartesian coordinates definition for the laminar inflow cases. Defined as the origin, the rotor is positioned at $2.5D_0$ downstream from the inflow boundary and is centered in the yz plane. Within this domain, levels of refined mesh are arranged in a cylindrical shape with diameters of $3D_0$, $2D_0$, and $1.44D_0$ for different refinement levels. Grids are generated using `snappyHexMesh`, containing 10.6 million cells. As for the turbulence inflow case, the domain extends to $6D_0$ upstream with a refined region at the inflow, resulting in 12 million cells. This modification accounts for the development of the flow and helps mitigate undesired pressure fluctuations caused by the synthetic turbulent inlet. At the most refined level in both mesh layouts, the grid size $\Delta/R_0 \approx 1/40$ within the range suggested by Jha et al. (2014).

The choice of spatial differencing scheme for the convective term influences energy dissipation levels in the simulation. It is well-known that upwind schemes introduce numerical diffusion, while central difference schemes can lead to dispersion errors. To balance preserving wake structures and mitigating numerical oscillations, a blended scheme has been employed (Ivanell et al., 2010; Jha et al., 2014). The blended scheme was carried out by the `Gauss fixedBlended` with 95% `cubic` and 5% `upwind`.

The time step Δt is set at 1.4×10^{-2} s, corresponding to a 1-degree rotor rotation. This results in a Courant-Friedrichs-Lewy number of 0.09. At each time step, the Navier Stokes equations are iteratively solved by `pimpleFoam` and march with a blended scheme using 90% of `Crank-Nicolson` and 10% of `Euler`, and the tolerance is set to be 10^{-6} for both pressure and velocity fields. The simulation was set to run for 120 rotor revolutions, corresponding to approximately 600 s.

2.4 Blade truncation and effective diameter

The rotor asymmetry is introduced by blade length difference. One of the blades $R_{\Delta r}$ was truncated, leaving the other unmodified R_0. Besides, rotational imbalance is not considered, since no mass and shaft are applied in the actuator lines method. The blade truncation is implemented in the ALM by reducing the number of blade elements to control the spacing Δ_b. Based on the current discretization of the actuator line, the blade length difference $\Delta r^* = \Delta r/R_0$ is imposed to vary from the baseline 0% to 30% in increments of 2.5%, with each step corresponding to the removal of one blade element.
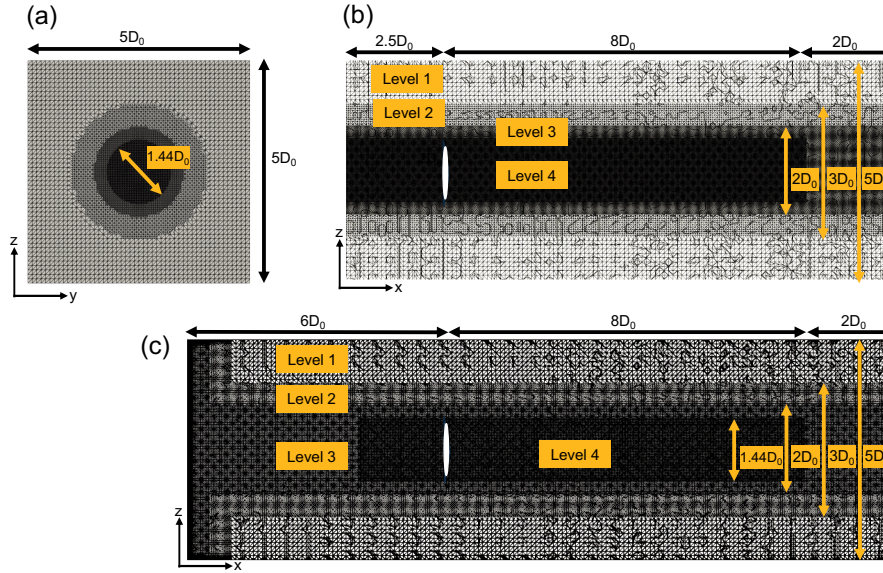
Figure 2. Mesh layout (a) yz plane and xz plane under (b) laminar inflow and (c) turbulent inflow condition. White strips indicate the rotor model.

The overall performance decreases due to the truncation of one blade, although the frontal area of the modified turbine remains unchanged. Given that performance coefficients in wind energy fields are conventionally normalized by area, the effective swept area A_e is defined as the average of the original swept area and the swept area by the truncated blade. Conse-
145 quently, the relation between D_e and D_0 can be obtained as Eq. 6. With this definition, the effective diameter D_e serves as a bulk length scale for wake statistics, while D_0 is used for analyzing tip vortex behavior, reflecting the physical position. Unless otherwise noted, the properties are normalized by D_0 and U_∞, marked with an asterisk, including streamwise x^* and radial positions z^*, as well as vorticity ω_y^* and time-averaged velocity $\overline{u}^*$. The diagram of blade truncation, its implementation on the actuator line, and the resulting effective diameter are illustrated in Fig. 1 (a).

150 $$D_e = D_0 \sqrt{1 - \Delta r^* + \frac{\Delta r^{*2}}{2}} \tag{6}$$

Table 1 presents the effective diameters for various blade length differences, along with the corresponding (effective) thrust and power coefficients. The original performance data are obtained from the LES-ALM results. For the effective performance coefficients, A_0 is replaced with A_e during normalization. The similarity in resulting $C_{T,e}$ and $C_{P,e}$ values across different Δr^* indicates that the proposed length scales can effectively normalize rotor size by performance.

WIND
ENERGY
SCIENCE
DISCUSSIONS

Table 1. (Effective) performance with blade length differences

$\Delta r^*[\%]$	D_e/D_0 [-]	Performance		Effective Performance	
		C_T	C_P	$C_{T,e}$	$C_{P,e}$
0.0	1.00	0.543	0.426	0.543	0.426
2.5	0.99	0.532	0.417	0.546	0.427
5.0	0.98	0.520	0.407	0.546	0.427
7.5	0.96	0.508	0.397	0.546	0.427
10.0	0.95	0.494	0.387	0.545	0.427
12.2	0.94	0.482	0.377	0.544	0.426
14.6	0.93	0.470	0.368	0.544	0.426
17.1	0.92	0.458	0.360	0.543	0.425
19.5	0.91	0.447	0.351	0.543	0.426
29.3	0.87	0.405	0.321	0.540	0.428

3 2D point vortex model

In the literature, there are several approaches to define the growth of leapfrogging instability. Widnall (1972), Gupta and Loewy (1974), Ivanell et al. (2010) and Sarmast et al. (2014) analyzed the relevant modes in the frequency domain, while Bolnot (2012) and Quaranta et al. (2019) conduct their studies in the time domain. The current study also investigates the growth rate in the time domain, with a different definition.

In Bolnot (2012) and Quaranta et al. (2019), the growth rate of the instability is defined based on the difference in the separation distance between a vortex and its two neighboring ones. Although this method calculates a growth rate of $\pi/2$ following findings in Sarmast et al. (2014); Selçuk et al. (2017), this definition only considers the streamwise separation between a vortex pair. However, the pairing motion also displaces the vortex in the radial direction. Hence, an alternative definition is proposed to consider two degrees of freedom, both streamwise and radial vortex separation. This method is based on a general point vortex row model introduced by Aref (1995), but specializes in a zero-wavenumber perturbation and focuses on the temporal variation of separation distance between vortex pairs. Moreover, this definition only requires the information from vortex pairs rather than trios, simplifying post-processing and expanding the available data field.

3.1 Model definition

This model consists of two parallel arrays of vortices, separated by an initial radial distance Δr in the z-direction and aligned along the x-axis (streamwise). Each array is uniformly spaced with a helical pitch of $2h_0$ as an initial condition, establishing a streamwise distance of h_0 between staggered vortices from the two arrays. This arrangement models the tip vortices shed from two rotor blades of different lengths, and the smallest unit in this model is illustrated in Fig. 3.
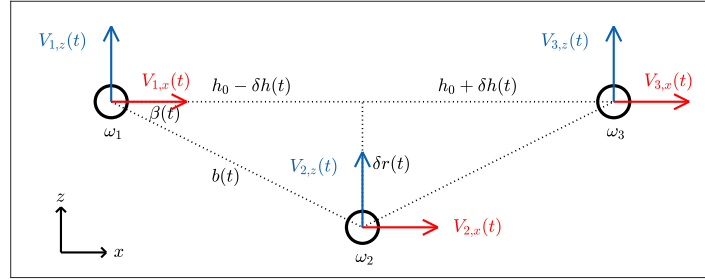
Figure 3. Diagram of a smallest unit in 2D point vortex model

$$
\frac{d}{dt}\begin{bmatrix} \delta x_i \\ \delta z_i \end{bmatrix} = \begin{bmatrix} V_{i,x} \\ V_{i,z} \end{bmatrix} = \begin{bmatrix} \frac{\Gamma}{2\pi} \sum_{j=1, j\neq i}^{2N_p} \frac{z_j - z_i}{(x_j - x_i)^2 + (z_j - z_i)^2} \\ \frac{\Gamma}{2\pi} \sum_{j=1, j\neq i}^{2N_p} \frac{x_j - x_i}{(x_j - x_i)^2 + (z_j - z_i)^2} \end{bmatrix} \tag{7}
$$

The dynamics of the i vortex in the x and z directions are determined by the velocities $V_{i,x}$ and $V_{i,z}$, which are the sums of the induction from all other vortices (Anderson, 2017), as shown in Eq. 7. The circulation Γ is assumed constant across the arrays, and the index j ranges from 1 to $2N_p$, where N_p denotes the number of vortices on both sides of the i vortex in $\pm x$ directions.

$$
\frac{d}{dt}\begin{bmatrix} \delta h \\ \delta r \end{bmatrix} = \begin{bmatrix} 2V_x(\delta h, \delta r) \\ 2V_z(\delta h, \delta r) \end{bmatrix} \tag{8}
$$

The magnitude of induced velocity is identical for both arrays and assumed uniform across all vortices, i.e., $V_x = |V_{i,x}|$ and $V_z = |V_{i,z}|$. Specifically, given a positive Γ in y-direction, ω_1 and ω_3 in Fig. 3 travel with $+V_x$ and $+V_z$, while ω_2 travels with $-V_x$ and $-V_z$. This results in the pairing motion of ω_1 and ω_2, and the same occurs for the rest of the vortex array. Consequently, the variation of separation between the vortex pair streamwise δh and radial δr change at rates of twice V_x and V_z, as described in Eq. 8.

A system with δh and δr serves as the governing equations for the 2D point vortex model. This formation offers two main advantages. Firstly, the synchronous displacement across the vortex array ensures identical temporal evolution for any pair, simplifying studies on vortex pairing growth rates to just one representative pair. Secondly, focusing on the variation between vortex pairs instead of individual positions reduces the system's degree of freedom.
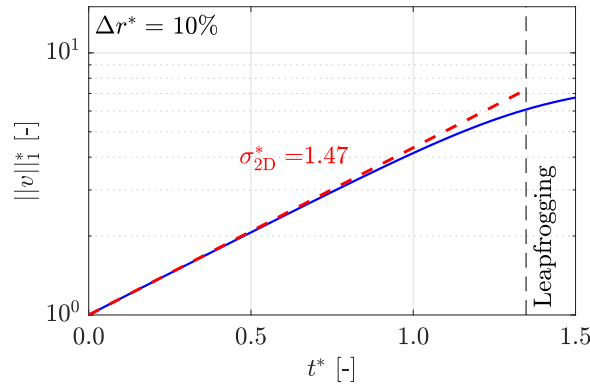
Figure 4. Temporal growth of $||v||_1^*$ from 2D vortex model in an example of $\Delta r^* = 10\%$

3.2 Leapfrogging instability

As derived in the previous subsection, Eq. 8 describes the vortex pairing motion due to the misalignment of two vortex arrays
of a non-linear system. Applying a Taylor expansion for linearization makes this system an eigenvalue problem, as in Eq. 9,
where $\mathbf{J}$ denotes the Jacobian matrix.

$$\frac{d}{dt}\begin{bmatrix} \delta h \\ \delta r \end{bmatrix} = \mathbf{J}\begin{bmatrix} \delta h \\ \delta r \end{bmatrix} \xrightarrow{\text{Solve for Eigenvalues}} \begin{bmatrix} \delta h \\ \delta r \end{bmatrix} = c_1 e^{\sigma_1 t}\boldsymbol{v_1} + c_2 e^{\sigma_2 t}\boldsymbol{v_2} = c_1 e^{\sigma_1 t}\begin{bmatrix} 1 \\ 1 \end{bmatrix} + c_2 e^{\sigma_2 t}\begin{bmatrix} 1 \\ -1 \end{bmatrix} \tag{9}$$

By solving the eigenvalue problem, two modes are obtained with real eigenvalues of opposite signs, where $\sigma_1 = -\sigma_2 > 0$.
This eigenvalue set indicates that the first mode is unstable and expected to grow exponentially over time, while the second
mode decays. Here, σ_1 is served as the growth rate of the unstable mode. Furthermore, the resulting eigenvectors $\boldsymbol{v_1} = [1;1]$
and $\boldsymbol{v_2} = [1;-1]$ suggest that the unstable mode grows along the 45 degrees between δh and δr. Given the obtained eigenvector
pair, the L1 norm of δh and δr isolates the unstable mode in the system. The normalized L1 norm $||v||_1^*$, by the initial condition,
is therefore expected to grow exponentially in time from unity, as shown in Eq. 10

$$||v||_1^* = \frac{\delta h + \delta r}{\Delta r} = e^{\sigma_1 t} \tag{10}$$

Nonetheless, such linearization is not applicable when Δr^* cannot be considered as a small perturbation, where the initial
conditions are far from the equilibrium point. Therefore, an alternative approach involves performing numerical integration on
the nonlinear system (Eq. 8) using `ode45` function in MATLAB®. Figure 4 presents the L1 norm from the integrated result of
$\Delta r^* = 10\%$ in normalized time, defined as $t^* = t\Gamma/h_0^2$ (Selçuk et al., 2017; Quaranta et al., 2015). The exponential growth of
$||v||_1^*$ is observed by the linear part under a semi-log scale. The slope of this part defines the growth rate of the leapfrogging
instability, denoted as σ_{2D}^*. Furthermore, the normalized leapfrogging time t_{LF}^* is defined where the vortex pair swap their
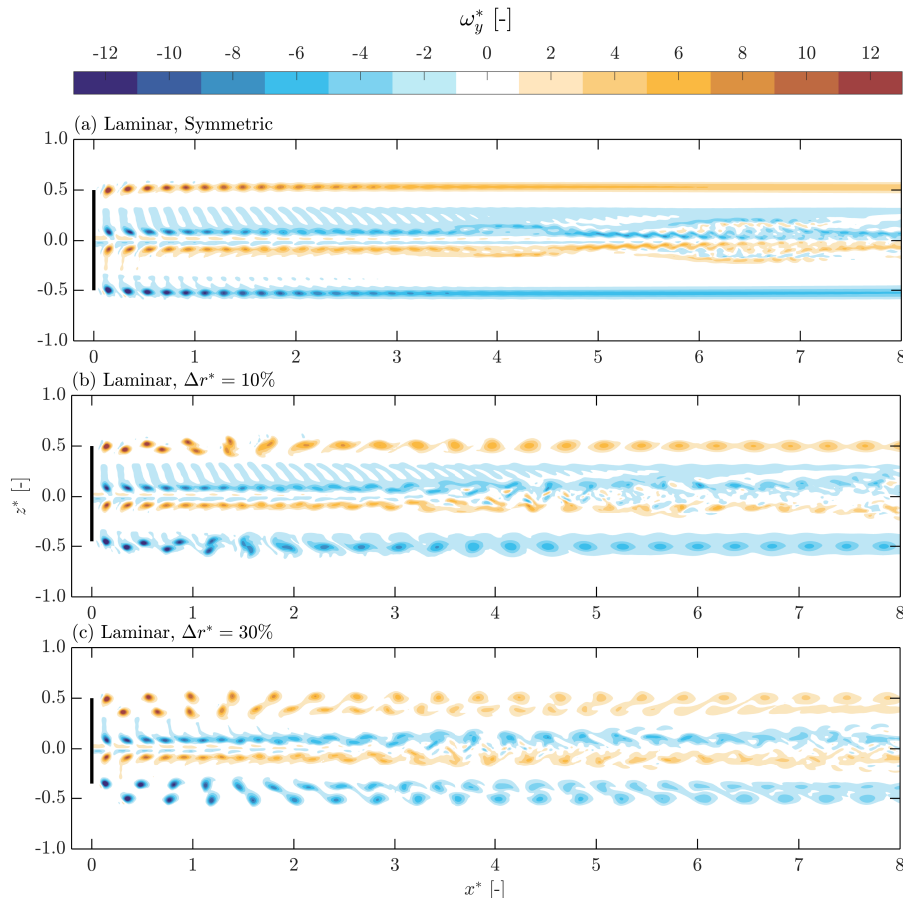streamwise positions, namely when $h_0 = \delta h$, marked by the dashed line in Fig. 4.

Figure 5. Vorticity-y contours under laminar inflow condition and different Δr^*s

4 Results and discussion

Figure 5 and 6 show the instantaneous vorticity fields for $\Delta r^* = [0\%, 10\%]$ under a laminar inflow condition and a turbulent inflow, respectively, where an extreme case of $\Delta r^* = 30\%$ is also shown in Figure 5.

4.1 Tip vortex behavior under laminar inflow

Under laminar conditions, with a symmetric rotor, the vortices are released at the blade tip and convected downstream along aligned trajectories. It is only after $4D_0$ downstream that the independent vortex cannot be distinct, leaving a trace of the vorticity in the form of a stable shear layer (Fig.5(a)). This condition is purely illustrative, but it may never be verified in practice, given the typical values of the Reynolds number, where transitional and turbulent behavior is expected, that will prevail in the laminar development of the wake flow.
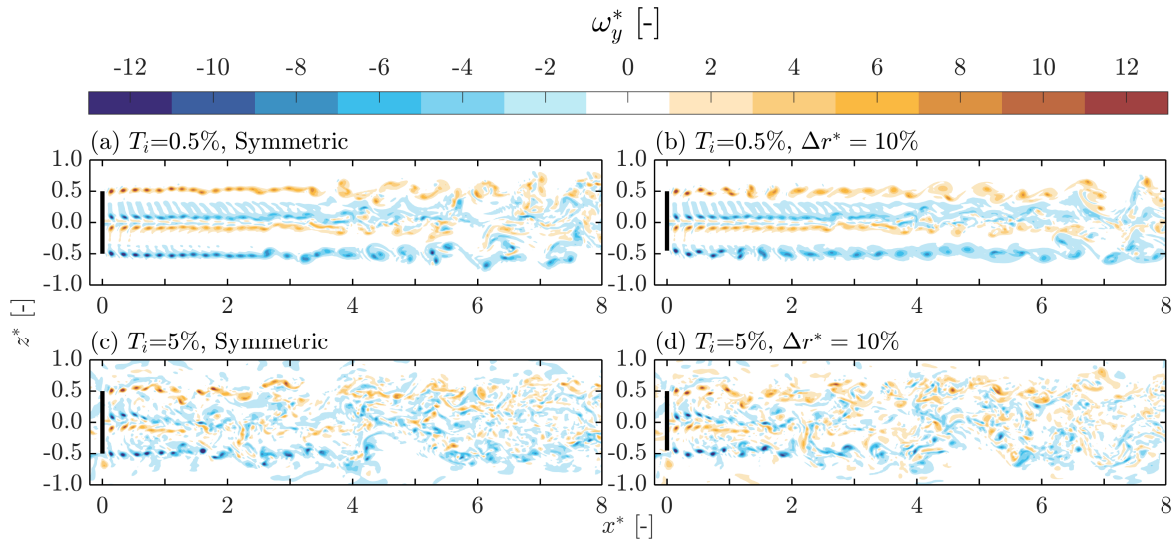
Figure 6. Vorticity-y contours under turbulent inflow conditions and different Δr^*. The black lines indicate the actuator line model.

When a blade length difference of 10% is introduced (Fig.5(b)), tip vortices are released at a different radial position. Given their vorticity, the vortex-induced velocity, according to Biot-Savart law causes the outer vortices to surpass the inner ones. This process leads to the condition of maximum proximity, when they can pair, whereby the relative motion streamwise is coupled to a vertical motion too. The overall effect is that of a precession of the vortex pair around a common point of rotation. As the pairing process advances, the vortices approach one another and eventually merge, forming a single, larger vortex. The above observations are consistent with the mechanisms identified and discussed in the literature (Selçuk et al., 2017; Ramos-García et al., 2023), where vortex pairing and merging were demonstrated under similar conditions. When a significantly larger blade length difference is considered (up to 30%, Fig.5(c)) the radial distance between the vortices is such that pairing process does not occur. At such increased vortex separation Δr^*, the vortex-induced velocity is weaker (Biot-savart law predicts the inverse of the distance) and a longer interaction time is necessary to integrate the effect of the neighbouring vortex. Furthermore, the difference in convective velocity between the outer and inner vortices reduces the time available to integrate the induced velocity into a mutual displacement. The overall result is that even when vortices are approximately at the same vertical position (condition of minimum distance) the precession motion is not triggered and the outer vortices continue their motion, practically unaltered, along the streamwise direction. In conclusion, an excessive difference between blades causes the leapfrogging not to be followed by vortex merging.

4.2 Turbulent inflow conditions

When considering a minor level of turbulence in the incoming stream ($T_i = 0.5\%$), the pairing pattern in the near wake ($x^* < 2$) is essentially unaltered (Fig. 6 (a)(b)). However, due to the turbulent fluctuations, the vortices feature some random displacements. The latter grow downstream, resulting in fluctuations at larger-scale. Such instability grows significantly around
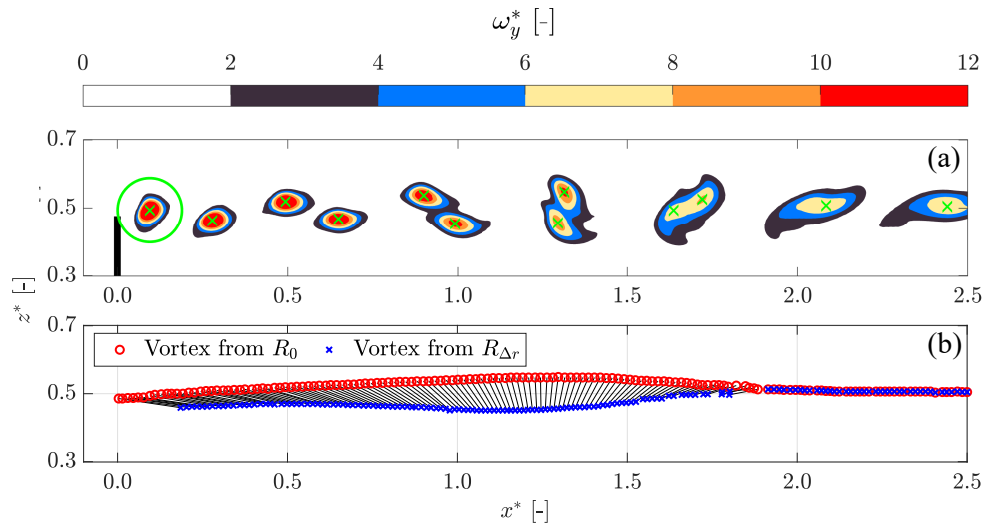
Figure 7. (a) Vorticity contour at top tip height at a single time step and (b) Vortex trajectory in an example of $\Delta r^* = 10\%$, where black lines mark the separation distance b between vortices shed from blades of different lengths at the same time step.

235 $4D_0$ and more downstream, the system of tip vortices is observed to break down into chaotic motions, resembling that of a turbulent wake.

When an atmospheric boundary layer turbulence level of $T_i = 5\%$ is considered at the inflow, the vorticity field exhibits a less regular pattern and in particular it affects the development of the helical vortex wake. In both the symmetric case (Fig. 6 (c)), and the asymmetric case (Fig. 6 (d)), the small-scale turbulence structures can be observed both the in free stream and within the

240 wake. Initially, the tip vortex structure remains similar to that observed in the laminar case and with $T_i = 0.5\%$. However, the higher turbulent fluctuations cause the tip vortex behavior to deviate after $1D_0$, leading to a faster wake breakdown. As a result, the tip vortex core becomes less distinct. Overall, the precession behavior in the near wake follows the rotor configuration, while the wake helix stability is dominated by T_i.

4.3 Vortex pair trajectory

245 Vortex properties and trajectories are evaluated at the tip height to analyze the leapfrogging mechanism. The initial vortex property is measured to determine leapfrogging instability's characteristic length and time scale. Figure 7(a) illustrates the situation, indicating the vorticity centroids by green markers. First, the vortex is placed at the point of maximum vorticity (Troldborg, 2009), followed by the determination of h_0. Second, the circulation is obtained, evaluating a surface integral of vorticity over a circular region, with a diameter h_0 (Ramos-García et al., 2023). This approach prevents overlapping of

250 neighbouring control surfaces. As shown in Table 2, the resulting vortex properties reveal a negligible discrepancy (<1%) in terms of circulation among different blades, which consolidates the assumption of uniform circulation in the 2D vortex model.

Table 2. Initial vortex properties measured from LES ALM - Laminar data

Property	Value
Γ_{R_0}	$(100.5 \pm 1)\ \mathrm{m^2 s^{-1}}$
$\Gamma_{R_{\Delta r}}$	$(99.5 \pm 0.4)\ \mathrm{m^2 s^{-1}}$
h_0	23.5 m
h_0/D_0	0.189

Vortex trajectories are obtained reverting to a technique commonly used in particle tracking velocimetry techniques (Raffel et al., 2018), assuming that the vortex travels as a whole and its centroid can be always identified. With the initial centers of the latest vortices shed from different blades, the motion is tracked by identifying the nearest neighbors within a search radius around the expected position in the subsequent time frame. This procedure is repeated exploring all the vortices present in the domain. The resulting trajectory of the vortex pair, for example of $\Delta r^* = 10\%$, is presented in Fig. 7(b). The spatio-temporal development of the vortex pair's behavior is depicted, which returns in this case the precession motion (leapfrogging), followed by merging.

Following the notations defined in the 2D vortex model (Fig. 3), the evolution of the normalized relative distance between pairing vortices is displayed in Fig. 8. The angle between the vortex pair relative to the streamwise direction β (Fig. 8 (a)), separation distance b (Fig. 8 (b)), and its streamwise projection $h_0 - \delta h$ (Fig. 8 (c)) and radial δr (Fig. 8 (d)) one are plotted against the streamwise location of the vortex pair's centroid, where the distances are normalized by D_0.

The leapfrogging and merging distances can be determined from β (Fig. 8 (a)) and b (Fig. 8 (b)). First, an increasing value of β suggests that the outer vortex gradually surpasses the inner one. The condition when β reaches 90 degrees indicates that the vortex pair is aligned in the radial direction, such location is identified as the leapfrogging distance, x_{LF}. Secondly, the decrease in b indicates that the vortices approach one another as they travel downstream. When only a single vorticity peak can be detected within the search radius, b eventually drops to zero. This defines x_{Merg}, the merging distance. Note that before merging, only one leapfrogging event can be observed.

The projection of b along the streamwise and radial directions are $h_0 - \delta h$ and δr, plotted in Fig. 8 (c)and (d), respectively. First, the streamwise separation decreases from h_0 to -0.1D_0 and drops to zero at x_{Merg}. Before the merging point, a sign switch is observed at x_{LF}, indicating the radial alignment of the vortex pair and consistent with the finding from β evolution. Second, δr is observed to increase from around $0.03D_0$ and reaches a maximum at around x_{LF}, and then gradually decreases to zero at x_{Merg}.

The initial δr is expected to be the imposed radial offset Δr. However, a discrepancy around $0.02D_0$ between the initial δr and Δr is noticed, which may be ascribed to the process of wake expansion. Specifically, when the later vortex is shed from the original blade, the preceding vortex from the truncated blade has already traveled outward, decreasing the radial separation between them. Besides, the increment of δh is almost twice that of δr, suggesting that the evolution is not solely determined by mutual induction, where a similar variation would be expected according to the Biot-Savart law.
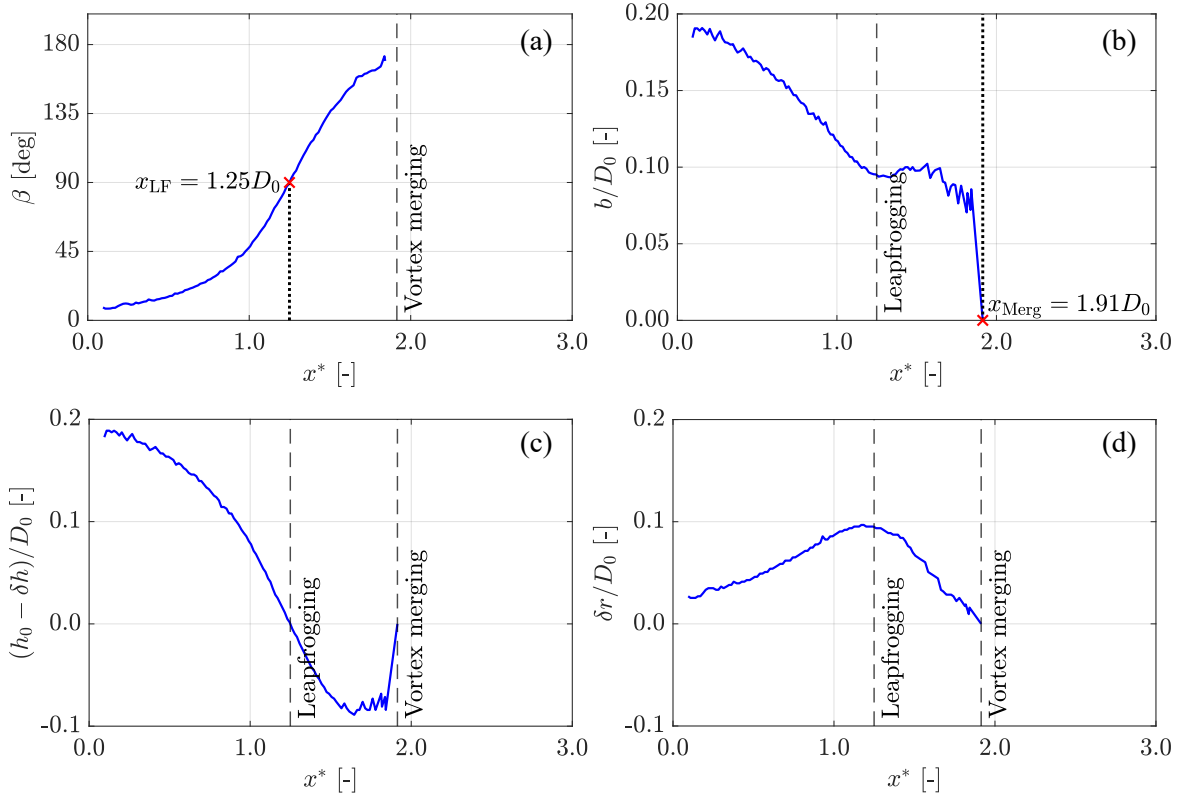
Figure 8. Spatial evolution relative position between vortex pair in the example of $\Delta r^* = 10\%$

4.4 Leapfrogging instability growth rate

280 As defined in Sect. 3, the instability growth rate is determined based on the L1 norm of the measured δh and δr. Figure 9 presents a semi-log plot of $||v||_1^*$ against the normalized time, which is converted from the vortex pair centroid by the convective velocity (Abraham et al., 2023a). A monotonic increase before t_{LF}^* and a linear region can be identified, indicating that the proposed methodology effectively captures the exponential growth of the leapfrogging instability. This linear phase follows a transient part and then transitions into a more gradual increase. This behavior compare favorably with the evolution

285 of streamwise separation reported by Bolnot (2012) and Quaranta et al. (2019), although the L1 norm definition is further supported by analytical formulations from the 2D point vortex model.

Moreover, the slope of this linear region is defined as the dimensionless instability growth rate (Quaranta et al., 2019), denoted as σ^*. The obtained the growth rate σ^* under different T_i and Δr^*, as well as σ_{2D}^*, are plotted in Fig. 10. The above evaluation is repeated considering 26 pairs of vortices in order to yield statistically significant values. The values are found to

290 repeat rather regularly, with random fluctuations among events of less than 3% under laminar and $T_i = 0.5\%$ inflow conditions, and up to 20% under $T_i = 5\%$ inflow conditions.
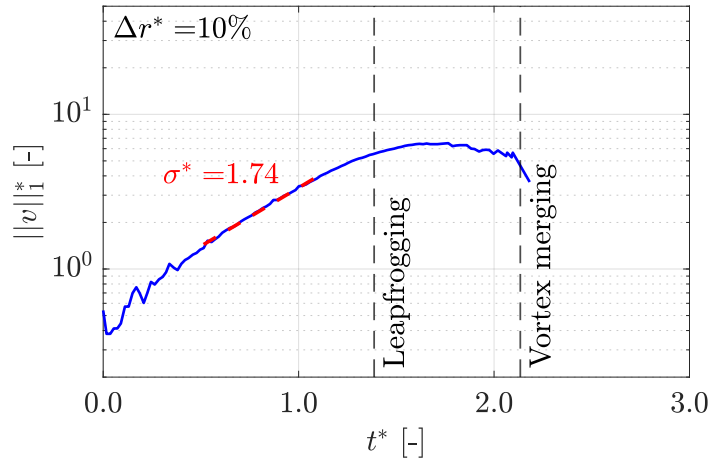
Figure 9. Temporal evolution of $||v||_1^*$ from results in the example of $\Delta r^* = 10\%$

Under laminar inflow conditions, σ^* (red crosses in Fig. 10) is observed to decrease with Δr^* from 1.9 to 1.3. This decrease indicates a comparison of the vortex-induced velocity and the difference in convection. As discussed in Subsect. 4.1, besides vortex-induced velocity, the difference in convective velocity between two tip vortices also plays a role in tip vortex behavior.

295 Specifically, the flow shear accelerates the increase in δh, thereby contributing positively to σ^*. This positive contribution is expected to be more pronounced with larger imposed Δr^*. Conversely, under such conditions, the vortex-induced velocity diminishes due to the increased separation distance between the vortex pairs, as predicted by the Biot-Savart law, resulting in a negative contribution to σ^* as Δr^* increases. The observed decrease in σ^* suggests that the positive contribution from velocity differences is less pronounced than the negative impact of reduced induction.

300 Furthermore, the turbulent intensity has a marginal influence on σ^*. When 0.5% T_i is introduced, the mean value of σ^* differs up to 3% than that in the laminar case. With 5% T_i, due to the turbulent fluctuation, σ^* are at most 7% larger but more scattered with the standard deviation shown as error bars.

A similar decreasing trend is observed in the growth rate from the 2D vortex model, σ_{2D}^* (black line in Fig. 10). As Δr^* approaches zero, σ_{2D}^* converges to 99.9% of $\pi/2$ with $N_p = 52$. Then, it gradually decreases to 1.25 as Δr^* increases to 20%,

305 attributed to the larger vortex separation. Besides, it is no surprise that there is a slight deviation between σ_{2D}^* and σ^*, as the 2D vortex model does not account for 3D effects, convection velocity, or wake expansion. Specifically, σ^* deviates from σ_{2D}^* by 17% at $\Delta r^* = 2.5\%$, and this deviation decreases to 5% at $\Delta r^* = 19.5\%$.

4.5 Leapfrogging distance and time

Leapfrogging distances x_{LF} are measured from LES-ALM data by the methods illustrated in Fig. 8(b) under different inflow

310 conditions and degrees of rotor asymmetry. Figure 11 reports the normalized leapfrogging distance x_{LF}^* against Δr^* from 2.5% to 20%.
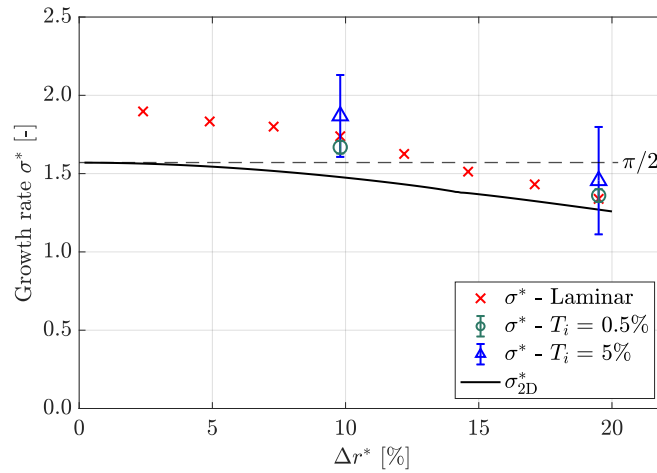
Figure 10. Comparison of growth rates obtained with different T_i and Δr^* from LES-ALM and 2D vortex model
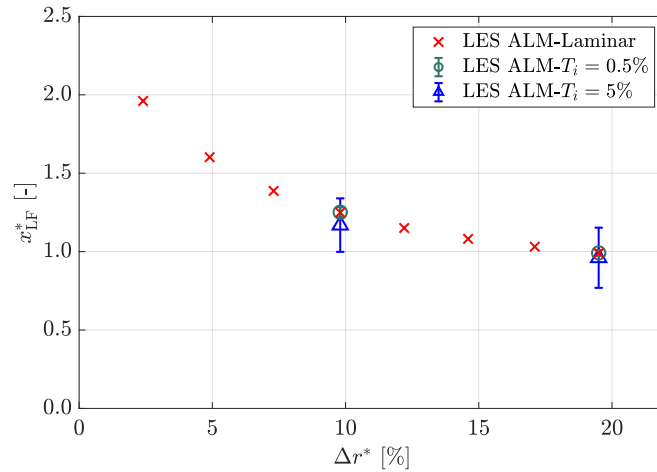

Figure 11. Leapfrogging distance under different Δr^* and inflow conditions from LES-ALM results

Under laminar inflow condition (red crosses in Fig. 11), x_{LF} decreases asymptotically from $2D_0$ and saturates around $1D_0$ as Δr^* increases from 2.5% to 19.5%. This trend suggests that the leapfrogging phenomenon occurs earlier with a greater rotor asymmetry, which compares well with the observation in Abraham and Leweke (2023). This is because a more developed form

315   of leapfrogging behavior is induced by a larger radial offset of the tip vortices, despite a smaller σ^*.

Besides, the contradicting trends between x_{LF} and σ^* can also be ascribed to their differing definitions. The leapfrogging distance is primarily determined by the streamwise separation between a vortex pair, $h_0 - \delta h$, which is influenced by both the difference in convective velocity and vortex-induced velocity. In contrast, the growth rate σ^* also accounts for the radial
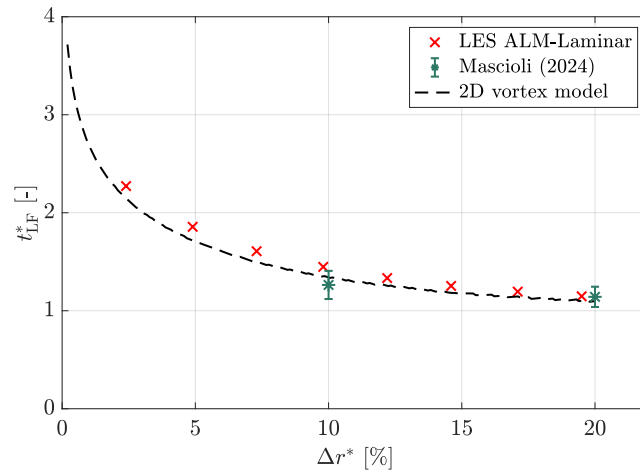
16

Figure 12. Comparison of leapfrogging time from LES-ALM results, 2D vortex model, and wind tunnel experiment (Mascioli, 2024).

component, which is predominantly governed by the vortex-induced velocity. As discussed in the previous subsection, vortex-induced velocity decreases with an increasing Δr^*. Consequently, as long as the influence of convective velocity differences persists, x_{LF} will not necessarily follow the same trend as σ^*.

Turbulence intensity T_i is found not to have a determining effect on the leapfrogging distance. The leapfrogging distances under 0.5% T_i (green circles in Fig. 11) are rather similar to those obtained under laminar inflow conditions. Secondly, at a higher turbulence intensity of 5% (blue triangles in Fig. 11), the data become more scattered, with mean values of x_{LF} being at most 6% lower than those under laminar conditions. To conclude, the minimal deviation in x_{LF} and σ^* between laminar and turbulent inflow conditions suggests that turbulent inflow has a minor effect on the near-wake tip vortex behavior, particularly regarding the leapfrogging phenomenon. It should, however, be kept in mind that flow turbulence will play an important role in triggering secondary instabilities of the vortex helix, as widely reported in the literature (Ivanell et al., 2010; Wang et al., 2022; Hodgkin et al., 2023).

The leapfrogging distances are subsequently converted to the normalized leapfrogging time t_{LF}^* by convection velocity, where the time scale offers a more general scale for comparison with the wind tunnel experiment (Mascioli, 2024) and the 2D vortex model. The transition from spatial and temporal is inspired by that proposed by Abraham et al. (2023a) and Quaranta et al. (2015), but with some adaptations needed for the present flow case, where their model considered the helix angle in determining the shortest vortex filament distance. In this study, the relatively large $\Delta r/h_0$ reduces the influence of the helix geometry. Figure 12 illustrates t_{LF}^* against Δr^*. The curve from the 2D vortex model shows good agreement with the LES ALM-Laminar data, with a difference of no more than 7% across the current Δr^* range. A similar level of agreement on leapfrogging was also observed in Abraham et al. (2023a) despite a simpler formation.

Furthermore, two data points from wind tunnel experiments (Mascioli, 2024) are also plotted, further supporting the agreement between the model and LES observations. The experiment was performed in the W-tunnel at TU Delft, using a 0.3 m
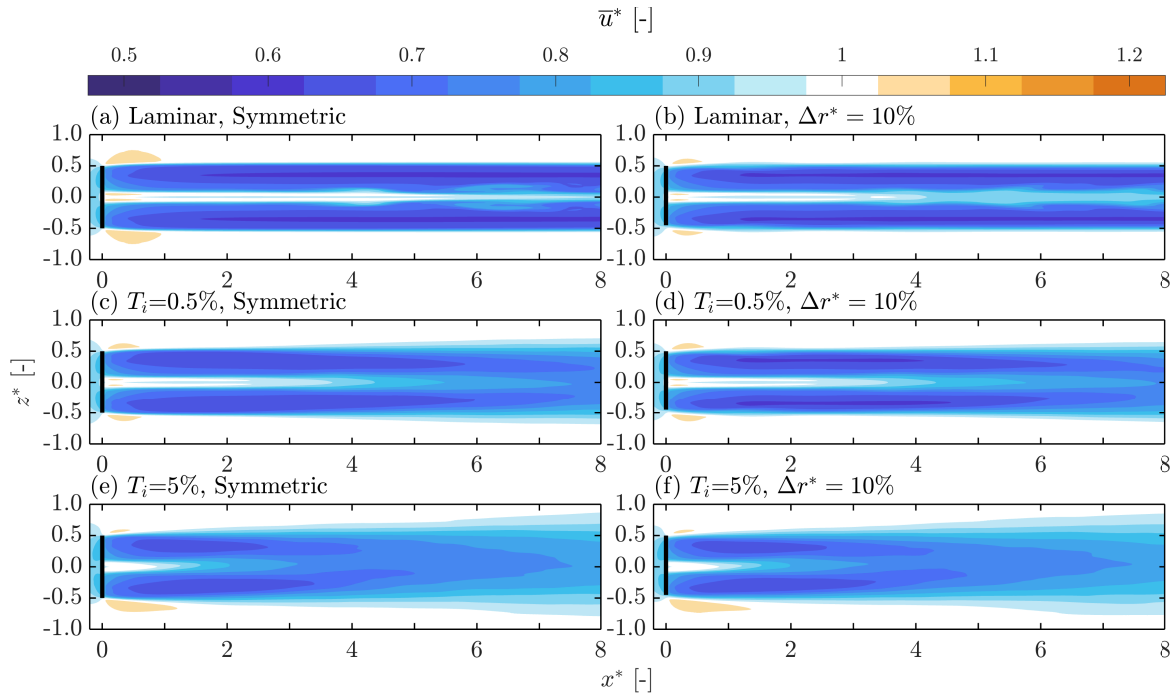
17

Figure 13. Streamwise mean velocity contour under different Δr^* and inflow condition

340 diameter, four-bladed rotor with an inflow velocity of approximately $5.4 \mathrm{~ms}^{-1}$. The tip speed ratio was set at 3.5, leading to a similar helix geometry $h_0/D_0 = 0.2$, and the resulting circulation of the tip vortices is around $0.08 \mathrm{~m^2s}^{-1}$. The consistency observed between the simulation and wind tunnel experiments suggests that both diameter- and circulation-based Reynolds numbers are not a determining factor in the leapfrogging phenomenon.

5   Results and discussion on wake characteristics

345 The streamwise evolution of the wake momentum is the relevant flow property to examine the wake characteristics during its recovery. The mean velocity $\overline{u}^*$ under different rotor configurations and inflow conditions is obtained from temporal statistics produced from a relatively long time interval of $60\,\mathrm{th}$ to $120\,\mathrm{th}$ revolution. The disk-averaged mean velocity $<\overline{u}>_{\mathrm{disk}}$, shows a deviation of $\pm\,10^{-5}\mathrm{~ms}^{-1}$ from the converging value under such averaging interval, which is equivalent to 0.03% relative to the greatest velocity difference across the wake boundary layer.

5.1   Streamwise mean velocity $\overline{u}^*$

Under laminar inflow conditions with a symmetric rotor, a higher velocity region downstream of the rotor tip, caused by rotor induction, is observed alongside a wake with a velocity deficit (Figure 13(a)). Besides, after the wake expansion behind the
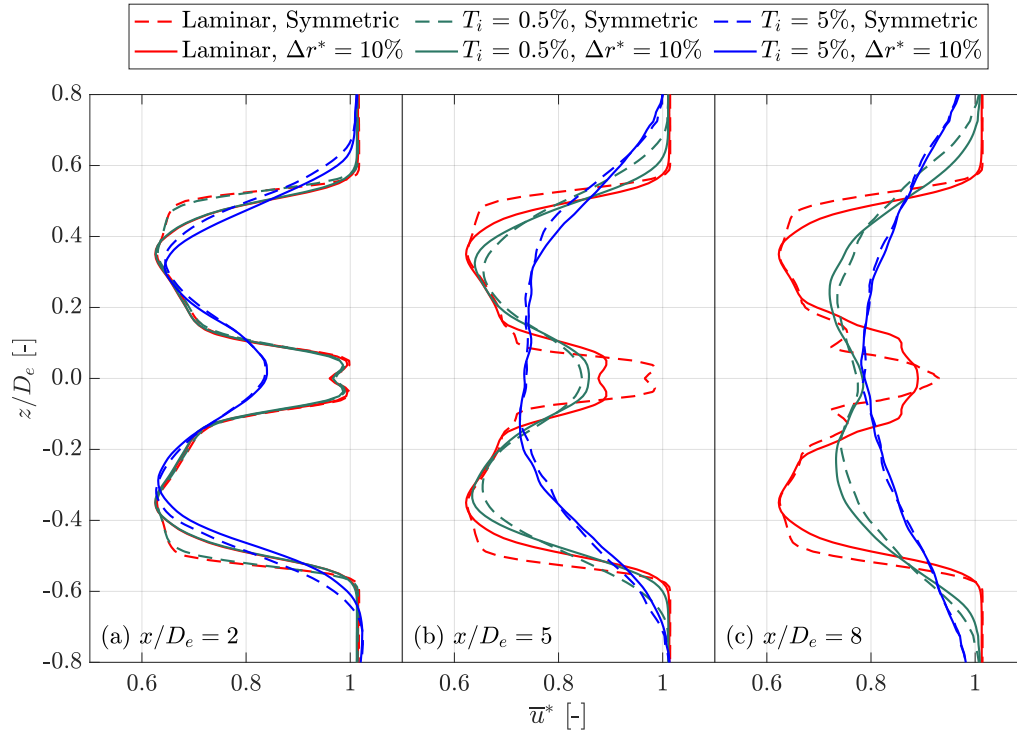
Figure 14. Streamwise velocity profiles under different Δr^* and inflow condition at $2D_e$, $5D_e$, and $8D_e$

rotor to $x^* = 1$, the shear layer remains stable further downstream, following the findings in Fig. 5 (a), where the unperturbed tip vortices formulate a stable shear layer. This behavior compares favorably with the observations in Li et al. (2024). On the other hand, when a 10% of Δr^* is introduced (Fig. 5 (b)), the shape of the boundary layer remains similar to the case of a symmetric rotor.

When considering 0.5% T_i at the inflow, the shear layer is observed to spread continuously downstream for both symmetric and asymmetric rotors (Fig. 13(c)(d)). At 5% T_i, the spread is even more pronounced (Fig. 13(e)(f)). Overall, up to $x^* = 8$, the wake deficit area is more affected by T_i than by Δr^*, with higher T_i leading to a more rapid spreading of the shear layer. As shown in Fig. 6, the increased turbulent fluctuations break down the tip vortex helix, which typically confines the wake (Medici, 2005), thereby allowing more powerful momentum exchange with the ambient flow and causing the velocity deficit to spread more in the radial direction, which in turn alleviates the maximum momentum deficit at the wake axis.

To further investigate the momentum deficit recovery, the velocity profiles at $2D_e$, $5D_e$, and $8D_e$ are shown in Fig. 14. At $2D_e$ (Fig. 14(a)), a typical turbine near-wake shape is observed across all cases, characterized by the lowest velocity at around 0.65 U_∞ and higher velocities near the hub. Strong velocity shear is evident in the tip and hub regions, where the loading is non-continuous. Additionally, the velocity profile shape follows the rotor configuration under laminar conditions (red lines)
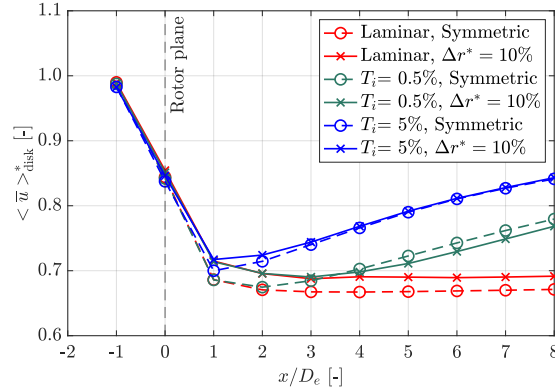
Figure 15. Nomralised leapfrogging distance under different Δr^* and inflow condition

and at $0.5\%\ T_i$ (green lines), with stronger shear observed at the tip for the symmetric rotor configuration. This is attributed to periodic loading variations at the tip region caused by the uneven blade lengths. However, as T_i increases to 5% (blue lines), the influence of rotor configuration becomes less pronounced. For both symmetric and asymmetric cases, the more gentle velocity profile gradient and a lower $\overline{u}^*$ are observed, indicating a stronger diffusion of velocity deficit.

370

The spatial evolution of wake is observed from the velocity profile at $5D_e$ and $8D_e$ downstream (Fig. 14(b) and (c)). Under laminar inflow conditions, changes can only be spotted at hub height for both symmetric and asymmetric rotor cases, where $\overline{u}^*$ decreases. The overall wake structure remains unchanged, consistently with the observation from the velocity contour(Fig. 13(a) and (b)), which showed that the wake undergoes minimal development as it travels downstream.

375

On the other hand, with a $0.5\%T_i$, the evolution towards well-known self-similarity (Porté-Agel et al., 2011) in the overall wake shape from $5D_e$ to $8D_e$ is evident. The concavities at the mid-span locations flatten due to turbulence-induced diffusion, with the symmetric rotor showing a slightly more advanced evolution, as the lowest $\overline{u}^*$ increases from 0.65 to 0.72. With a higher T_i of 5%, this diffusion becomes more pronounced, as expected. The inflection points in the velocity profile diminish, concavities merge into one, and the deficit diffuses further outward radially.

380 ## 5.2   Disk-averaged streamwise mean velocity $<\overline{u}>^*_{\text{disk}}$

The normalized disk-averaged streamwise mean velocity $<\overline{u}>^*_{\text{disk}}$ serves as a metric for evaluating wake recovery in this study. This metric is calculated by averaging the time-averaged streamwise velocity $\overline{u}$ over a circular disk with a diameter of D_e. Such an approach provides insight into overall streamwise velocity, estimating the wind resource available to the downstream turbine. Namely, more pronounced wake recovery is indicated by a more rapid increase in $<\overline{u}>^*_{\text{disk}}$ along the

385 streamwise direction.

Figure 15 plots $<\overline{u}>^*_{\text{disk}}$ at the downstream locations. For all cases, $<\overline{u}>^*_{\text{disk}}$ initially decreases to around 0.7 behind the rotor due to energy extraction. Under laminar conditions, only a slight increase is observed for both symmetric and asymmetric rotors, indicating minimal momentum recovery. With a $0.5\%\ T_i$, $<\overline{u}>^*_{\text{disk}}$ increases noticeably, especially with the symmetric

rotor. At 5% T_i, the increase is even more pronounced, but no significant difference is observed between the symmetric and

390   asymmetric rotor configurations.

The trend in $< \overline{u} >^*_{\text{disk}}$ is influenced more by T_i than by rotor configuration. With increasing T_i, the velocity recovers more rapidly, suggesting a more effective wake recovery, consistent with findings in the literature (Angelou et al., 2023; Li et al., 2016; Talavera and Shu, 2017). Combining the above findings and observations from Fig.5 and 6, one might relate the stability of the tip vortex helix with the wake recovery capability. Specifically, rotor asymmetry triggers the leapfrogging phenomenon

395   and merging, resulting in a new stable array composed of the smallest unit of two tip vortices. This is similar to the pattern observed in the symmetric rotor case, where the tip vortices array delays turbulent mixing with the free stream. Therefore, without a breakdown of the tip vortex helix, such as that induced by turbulent inflow or other mechanisms, wake recovery remains limited.

The findings above appear to contrast with the results reported by Lignarolo et al. (2015), who observed a sudden increase

400   in mean flow kinetic energy flux to the wake after leapfrogging. This discrepancy arises from the different factors leading to leapfrogging phenomenon. In the present numerical setup under laminar inflow, rotor asymmetry triggers only the zero-wavenumber perturbation (Gupta and Loewy, 1974). However, similar leapfrogging motion can also result from secondary instabilities, such as the local pairing observed in Quaranta et al. (2015), triggered by external perturbations such as ambient turbulence, breaking down the tip vortex helix coherence and periodicity (Hodgkin et al., 2023). This finding also appears

405   contradictory to the results of Abraham et al. (2023b), who, using vortex modeling, observed significant wake recovery following the leapfrogging event. This suggests that while the leapfrogging distance and growth rate are primarily governed by inviscid effects, which the vortex model can sufficiently capture—as demonstrated in this study—accurately quantifying the flow quantities in the complex vortex dynamics of an asymmetrical rotor still requires the use of a high-fidelity model.

6   Conclusions

410   The near wake behavior of a modified NREL 5MW wind turbine employing asymmetric rotors was investigated by means of LES in combination with the actuator line model. The rotor asymmetry was introduced by varying the blade length difference from 0% to 30%. The analysis is supported further by a simplified two-dimensional point vortex model.

The results show that rotor asymmetry accelerates the onset of leapfrogging, with the process occurring further upstream as the asymmetry increases. The leapfrogging time showed good agreement with both the 2D vortex model and wind tunnel

415   experiments (Mascioli, 2024). For blade length differences less than 20%, the two helical vortex sheets eventually merged, forming one larger vortex sheet. However, with more significant asymmetry, the increased vortex separation prevented the precession motion due to the lower induced velocity and the convective velocity difference between tip vortices.

The leapfrogging instability growth rate from LES results decreases with increasing blade length difference, aligning with the predictions of the 2D model. This decreasing trend indicates the positive contribution from velocity differences is less

420   pronounced than the negative impact of reduced induction. The apparent contradiction between the trends of leapfrogging time and growth rate arises from their different considerations. Leapfrogging time accounts only for the streamwise component,

which is influenced by both convective velocity and vortex-induced velocity. In contrast, the growth rate includes both the streamwise and radial components, with the radial component being governed solely by vortex-induced velocity.

Despite the early onset of leapfrogging triggered by rotor asymmetry, it was found to have minimal impact on the large-scale breakdown of the helix system and wake recovery, contrasting with the findings of Abraham et al. (2023b). After the leapfrogging and following the merging process, the resulting new stable vortex system indicated that other mechanisms are needed to accelerate the wake breakdown further. The above, may require verification through controlled experiments.

Finally, the inflow condition was found to have a minor effect on the induced near-wake tip vortex behavior by rotor asymmetry, as both the leapfrogging distance and growth rate remain rather unchanged when compared to those observed under laminar inflow. Inflow turbulence, however, is observed to play a major role in the process of wake recovery, overriding the effects of rotor asymmetry. In particular, the turbulent fluctuations induce the breakdown of the tip helical vortices, regardless of whether a symmetric or asymmetric rotor is used.

Code and data availability. Simulation data and post-processing codes are available upon request.

References

440 Abraham, A. and Leweke, T.: Experimental Investigation of Blade Tip Vortex Behavior in the Wake of Asymmetric Rotors, Experiments in Fluids, 64, https://doi.org/10.1007/s00348-023-03646-3, 2023.

Abraham, A., Castillo-Castellanos, A., and Leweke, T.: Simplified Model for Helical Vortex Dynamics in the Wake of an Asymmetric Rotor, Flow, 3, https://doi.org/10.1017/flo.2022.33, 2023a.

Abraham, A., Ramos-García, N., Sørensen, J.Nø., and Leweke, T.: Numerical Investigation of Rotor Asymmetry to Promote Wake Recovery,
445   in: Journal of Physics: Conference Series, vol. 2505, https://doi.org/10.1088/1742-6596/2505/1/012032, 2023b.

Anderson, J. D.: Fundamentals of Aerodynamics, McGraw-Hill Series in Aeronautical and Aerospace Engineering, McGraw-Hill Education, New York, NY, sixth edition edn., 2017.

Angelou, N., Mann, J., and Dubreuil-Boisclair, C.: Revealing Inflow and Wake Conditions of a 6 MW Floating Turbine, Wind Energy Science, 8, 1511–1531, https://doi.org/10.5194/wes-8-1511-2023, 2023.

450 Aref, H.: On the Equilibrium and Stability of a Row of Point Vortices, Journal of Fluid Mechanics, 290, 167–181, https://doi.org/10.1017/S002211209500245X, 1995.

Bachant, P., Goude, A., daa-mec, and Wosnik, M.: turbinesFoam/turbinesFoam: V0.1.1, Zenodo, https://doi.org/10.5281/zenodo.3542301, 2019.

Bolnot, H.: Instabilités des tourbillons hélicoïdaux: application au sillage des rotors, Thèse de doctorat, Aix-Marseille Université, 2012.

455 Brown, K., Houck, D., Maniaci, D., Westergaard, C., and Kelley, C.: Accelerated Wind-Turbine Wake Recovery Through Actuation of the Tip-Vortex Instability, AIAA Journal, 60, 1–13, https://doi.org/10.2514/1.J060772, 2022.

Gupta, B. P. and Loewy, R. G.: Theoretical Analysis of the Aerodynamic Stability of Multiple, Interdigitated Helical Vortices, AIAA Journal, 12, 1381–1387, https://doi.org/10.2514/3.49493, 1974.

Hansen, K. S., Barthelmie, R. J., Jensen, L. E., and Sommer, A.: The Impact of Turbulence Intensity and Atmospheric Stability on Power
460   Deficits Due to Wind Turbine Wakes at Horns Rev Wind Farm, Wind Energy, 15, 183–196, https://doi.org/10.1002/we.512, 2012.

Hodgkin, A., Deskos, G., and Laizet, S.: On the Interaction of a Wind Turbine Wake with a Conventionally Neutral Atmospheric Boundary Layer, International Journal of Heat and Fluid Flow, 102, 109 165, https://doi.org/10.1016/j.ijheatfluidflow.2023.109165, 2023.

Huang, X., Alavi Moghadam, S. M., Meysonnat, P. S., Meinke, M., and Schröder, W.: Numerical Analysis of the Effect of Flaps on the Tip Vortex of a Wind Turbine Blade, International Journal of Heat and Fluid Flow, 77, 336–351,
465   https://doi.org/10.1016/j.ijheatfluidflow.2019.05.004, 2019.

Ivanell, S., Mikkelsen, R., Sørensen, J. N., and Henningson, D.: Stability Analysis of the Tip Vortices of a Wind Turbine, Wind Energy, 13, 705–715, https://doi.org/10.1002/we.391, 2010.

Jha, P. K., Churchfield, M. J., Moriarty, P. J., and Schmitz, S.: Guidelines for Volume Force Distributions Within Actuator Line Modeling of Wind Turbines on Large-Eddy Simulation-Type Grids, Journal of Solar Energy Engineering, 136, https://doi.org/10.1115/1.4026252,
470   2014.

Jonkman, J., Butterfield, S., Musial, W., and Scott, G.: Definition of a 5-MW Reference Wind Turbine for Offshore System Development, Tech. Rep. NREL/TP-500-38060, 947422, National Renewable Energy Laboratory, https://doi.org/10.2172/947422, 2009.

Leishman, J., Bhagwat, M., and Bagai, A.: Free-Vortex Filament Methods for the Analysis of Helicopter Rotor Wakes, Journal of Aircraft, 39, 759–775, https://doi.org/10.2514/2.3022, 2002.

475 Li, Q., Murata, J., Endo, M., Maeda, T., and Kamada, Y.: Experimental and Numerical Investigation of the Effect of Turbulent Inflow on a Horizontal Axis Wind Turbine (Part II: Wake Characteristics), Energy, 113, 1304–1315, https://doi.org/10.1016/j.energy.2016.08.018, 2016.

Li, Y., Yu, W., and Sarlak, H.: Wake structures and performances of wind turbine rotor with harmonic surging motions under laminar and turbulent inflows, Wind Energy, 2024.

480 Lignarolo, L. E. M., Ragni, D., Scarano, F., Ferreira, C. J. S., and van Bussel, G. J. W.: Tip-Vortex Instability and Turbulent Mixing in Wind-Turbine Wakes, Journal of Fluid Mechanics, 781, 467–493, https://doi.org/10.1017/jfm.2015.470, 2015.

Lundquist, J. K., DuVivier, K. K., Kaffine, D., and Tomaszewski, J. M.: Costs and consequences of wind turbine wake effects arising from uncoordinated wind energy development, Nature Energy, 4, https://doi.org/10.1038/s41560-018-0281-2, https://www.osti.gov/biblio/1484339, 2018.

485 Martínez-Tossas, L., Churchfield, M., and Leonardi, S.: Large Eddy Simulations of the Flow Past Wind Turbines: Actuator Line and Disk Modeling, Wind Energy, 18, 1047–1060, https://doi.org/10.1002/we.1747, 2015.

Mascioli, A.: An experimental research of energy recovery in the wake of non-symmetrical rotors, Master's thesis, Università Roma Tre, 2024.

Medici, D.: Experimental Studies of Wind Turbine Wakes – Power Optimisation and Meandering, Tech. rep., KTH Royal Institute of Tech-
490 nology, 2005.

Mendoza, V., Chaudhari, A., and Goude, A.: Performance and Wake Comparison of Horizontal and Vertical Axis Wind Turbines under Varying Surface Roughness Conditions, Wind Energy, 22, 458–472, https://doi.org/10.1002/we.2299, 2019.

Odemark, Y. and Fransson, J. H. M.: The Stability and Development of Tip and Root Vortices behind a Model Wind Turbine, Experiments in Fluids, 54, 1591, https://doi.org/10.1007/s00348-013-1591-6, 2013.

495 Onel, H. C. and Tuncer, I. H.: Investigation of Wind Turbine Wakes and Wake Recovery in a Tandem Configuration Using Actuator Line Model with LES, Computers & Fluids, 220, 104 872, https://doi.org/10.1016/j.compfluid.2021.104872, 2021.

OpenFOAM Foundation: OpenFOAM User Guide: Version 2106, OpenFOAM Foundation, https://openfoam.org/release/2106/, 2021.

Poletto, R., Craft, T., and Revell, A.: A New Divergence Free Synthetic Eddy Method for the Reproduction of Inlet Flow Conditions for LES, Flow, Turbulence and Combustion, 91, 519–539, https://doi.org/10.1007/s10494-013-9488-2, 2013.

500 Porté-Agel, F., Wu, Y.-T., Lu, H., and Conzemius, R. J.: Large-Eddy Simulation of Atmospheric Boundary Layer Flow through Wind Turbines and Wind Farms, Journal of Wind Engineering and Industrial Aerodynamics, 99, 154–168, https://doi.org/10.1016/j.jweia.2011.01.011, 2011.

Quaranta, H. U., Bolnot, H., and Leweke, T.: Long-Wave Instability of a Helical Vortex, Journal of Fluid Mechanics, 780, 687–716, https://doi.org/10.1017/jfm.2015.479, 2015.

505 Quaranta, H. U., Brynjell-Rahkola, M., Leweke, T., and Henningson, D.: Local and Global Pairing Instabilities of Two Interlaced Helical Vortices, Journal of Fluid Mechanics, 863, 927–955, https://doi.org/10.1017/jfm.2018.904, 2019.

Raffel, M., Kähler, C., Willert, C., Wereley, S., Scarano, F., and Kompenhans, J.: Particle Image Velocimetry: A Practical Guide, Springer, 3rd edn., https://doi.org/10.1007/978-3-319-68852-7, 2018.

Ramos-García, N., Abraham, A., Leweke, T., and Sørensen, J. N.: Multi-Fidelity Vortex Simulations of Rotor Flows: Validation against
510 Detailed Wake Measurements, Computers & Fluids, 255, 105 790, https://doi.org/10.1016/j.compfluid.2023.105790, 2023.

Sarlak, H., Meneveau, C., and Sørensen, J. N.: Role of Subgrid-Scale Modeling in Large Eddy Simulation of Wind Turbine Wake Interactions, Renewable Energy, 77, 386–399, https://doi.org/10.1016/j.renene.2014.12.036, 2015.

Sarlak, H., Nishino, T., Martínez-Tossas, L., Meneveau, C., and Sørensen, J.: Assessment of Blockage Effects on the Wake Characteristics and Power of Wind Turbines, Renewable Energy, 93, 340–352, https://doi.org/10.1016/j.renene.2016.01.101, 2016.

515 Sarmast, S., Dadfar, R., Mikkelsen, R. F., Schlatter, P., Ivanell, S., Sørensen, J. N., and Henningson, D. S.: Mutual Inductance Instability of the Tip Vortices behind a Wind Turbine, Journal of Fluid Mechanics, 755, 705–731, https://doi.org/10.1017/jfm.2014.326, 2014.

Schröder, D., Aguilar-Cabello, J., Leweke, T., Hörnschemeyer, R., and Stumpf, E.: Experimental Investigation of a Rotor Blade Tip Vortex Pair, CEAS Aeronautical Journal, 13, 97–112, https://doi.org/10.1007/s13272-021-00555-1, 2022.

Selçuk, C., Delbende, I., and Rossi, M.: Helical Vortices: Linear Stability Analysis and Nonlinear Dynamics, Fluid Dynamics Research, 50,

520 011 411, https://doi.org/10.1088/1873-7005/aa73e3, 2017.

Shen, W. Z., Mikkelsen, R., Sørensen, J. N., and Bak, C.: Tip Loss Corrections for Wind Turbine Computations, Wind Energy, 8, 457–475, https://doi.org/10.1002/we.153, 2005.

Smagorinsky, J.: General Circulation Experiments with the Primitive Equations: I. The basic experiement, Monthly Weather Review, 91, 99–164, https://doi.org/10.1175/1520-0493(1963)091<0099:GCEWTP>2.3.CO;2, 1963.

525 Sørensen, J. N. and Shen, W. Z.: Numerical Modeling of Wind Turbine Wakes, Journal of Fluids Engineering, 124, 393–399, https://doi.org/10.1115/1.1471361, 2002.

Sørensen, J. N., Dag, K. O., and Ramos-García, N.: A Refined Tip Correction Based on Decambering, Wind Energy, 19, 787–802, https://doi.org/10.1002/we.1865, 2016.

Talavera, M. and Shu, a.: Experimental Study of Turbulence Intensity Influence on Wind Turbine Performance and Wake Recovery in a

530 Low-Speed Wind Tunnel, Renewable Energy, 109, 363–371, https://doi.org/10.1016/j.renene.2017.03.034, 2017.

Troldborg, N.: Actuator Line Modeling of Wind Turbine Wakes, Ph.D. thesis, Technical University of Denmark, 2009.

Troldborg, N., Larsen, G. C., Madsen, H. A., Hansen, K. S., Sørensen, J. N., and Mikkelsen, R.: Numerical Simulations of Wake Interaction between Two Wind Turbines at Various Inflow Conditions, Wind Energy, 14, 859–876, https://doi.org/10.1002/we.433, 2011.

van der Hoek, D., Frederik, J., Huang, M., Scarano, F., Simao Ferreira, C., and van Wingerden, J.-W.: Experimental Analysis of the Effect

535 of Dynamic Induction Control on a Wind Turbine Wake, Wind Energy Science, 7, 1305–1320, https://doi.org/10.5194/wes-7-1305-2022, 2022.

van Kuik, G. a. M., Peinke, J., Nijssen, R., Lekou, D., Mann, J., Sørensen, J. N., Ferreira, C., van Wingerden, J. W., Schlipf, D., Gebraad, P., Polinder, H., Abrahamsen, A., van Bussel, G. J. W., Sørensen, J. D., Tavner, P., Bottasso, C. L., Muskulus, M., Matha, D., Lindeboom, H. J., Degraer, S., Kramer, O., Lehnhoff, S., Sonnenschein, M., Sørensen, P. E., Künneke, R. W., Morthorst, P. E., and Skytte, K.: Long-

540 Term Research Challenges in Wind Energy – a Research Agenda by the European Academy of Wind Energy, Wind Energy Science, 1, 1–39, https://doi.org/10.5194/wes-1-1-2016, 2016.

Wang, L., Liu, X., Wang, N., and Li, M.: Propeller Wake Instabilities under Turbulent-Inflow Conditions, Physics of Fluids, 34, 085 108, https://doi.org/10.1063/5.0101977, 2022.

Widnall, S. E.: The Stability of a Helical Vortex Filament, Journal of Fluid Mechanics, 54, 641–663,

545 https://doi.org/10.1017/S0022112072000928, 1972.